Siu-Kit Lau[1]
Department of Architecture,
School of Design and Environment,
National University of Singapore,
4 Architecture Drive,
Singapore 117566
e-mail: slau@nus.edu.sg

Yong Zhao
Department of Architecture,
School of Design and Environment,
National University of Singapore,
4 Architecture Drive,
Singapore 117566

Stephen Siu Yu Lau
Department of Architecture,
School of Design and Environment,
National University of Singapore,
4 Architecture Drive,
Singapore 117566
e-mail: akilssy@nus.edu.sg

Chao Yuan
Department of Architecture, School of
Design and Environment,
National University of Singapore,
4 Architecture Drive,
Singapore 117566
e-mail: akiyuan@nus.edu.sg

Veronika Shabunko
Solar Energy Research Institute of Singapore,
National University of Singapore,
7 Engineering Drive,
Singapore 117574
e-mail: veronika.shabunko@nus.edu.sg

An Investigation on Ventilation of Building-Integrated Photovoltaics System Using Numerical Modeling

This study numerically investigates the thermal behavior and airflow characteristics of the building-integrated photovoltaic (BIPV) façade. A three-dimensional model is developed based on the typical BIPV façade. Computational fluid dynamics (CFD) with the shear stress transport (SST) κ-omega turbulent model is used in the study. The effects of geometric configurations on the BIPV cell temperature in steady state are evaluated including the sizes of the bottom and top openings and the depth of the back air cavity (or so-called cavity depth). When the sizes of the inlet and outlet openings are the same, the effects on the decrease of cell temperature are limited. By enlarging the bottom (inlet) opening, the impact of ventilation in the cavity behind is more significant and the cell temperature decreases. Cavity depth is also a vital factor affecting BIPV cell temperature. The paper identifies the optimal cavity depth of approximately 100–125 mm. Flow disturbance and a vortex may be observed at the bottom and top of the air cavity, respectively, as the cavity depth increases which negatively affects the ventilation causing these flow disturbances to increase the cell temperature. Thermal effects of environmental conditions are compared with regard to two selected BIPV configurations. The wind velocity and the attack angle also have an obvious impact on cell temperature. Ambient temperature and solar irradiance exhibit a linear relationship with BIPV cell temperature as expected.
[DOI: 10.1115/1.4044623]

Keywords: BIPV, CFD, ventilation, cooling, PV performance, temperature, design, environmental conditions, building, exergy, heat transfer, photovoltaics, renewable, simulation, sustainability

1 Introduction

In 2011, the world energy consumption stood at approximately 10 terawatts (TW) per annum, and it is projected to reach 30 TW by 2050 [1]. Buildings currently consume approximately 40% of the world's energy. With further urbanization, it is expected that energy consumption will increase due to the growing population and economy, as well as due to the energy demand for new buildings. The need for environmental sustainability calls for net-zero energy buildings and new renewable energy sources, for instance, solar energy. Recently, the potential of rooftop solar photovoltaic power in urban areas has been investigated [2,3]. However, in most buildings, rooftop photovoltaics (PV) alone cannot provide sufficient localized power generation that achieves a net-zero energy building. Façade integrations of photovoltaic systems or building-integrated photovoltaics (BIPV) offer a viable solution for a higher share of localized power generation [4].

Electrical conversion efficiency of PVs, however, depends on their operational temperature. Overheating may occur due to high cell temperatures of BIPVs when cooling effects from wind are low, and ventilation behind the modules is limited compared with the free-standing rooftop PV modules. Radziemska [5] investigated the temperature impact on the efficiency of crystalline silicon solar cell and determined that lower temperature of solar cells provides higher power output. As the temperature rises, a decrease may be observed of the output power (−0.65%/K), the fill-factor (−0.2%/K), and the conversion efficiency (−0.08%/K) of PV modules. In fact, PV panels absorb up to 80% of solar irradiation. A significant part of that energy will be converted into heat. For crystalline panels that are commonly used in the market, these result in a power generation drop of 0.45%/K [6,7]. Experimental studies show that power generation of a semi-transparent PV module decreases 0.48%/K in standard test conditions that do not account for temperature and 0.52% in outdoor conditions under 500 W/m^2 [8]. Overall, the electrical conversion efficiency of a PV module increases as the cell temperature decreases [9].

Numerous studies have been performed to evaluate the performance of the photovoltaic-thermal (PV/T) modules [10–14]. Air, water, or other media may be used for cooling and transferring heat of PV modules. Reclaimed heat can be applied for heating of space or water. Slimani et al. [14] performed a comparative study of thermal and electrical performance for four different PV/T air collectors. They concluded that wind velocity is an essential factor for high electrical efficiency. Also, the optimization of PV/Ts with air collectors has been investigated [15]. A parametric study indicated that PV/Ts with water collectors can increase cell efficiency by 5.3% [16]. Nahar et al. [17] proposed a pancake-shaped flow channel collector for PV/T. For every 100 W/m^2 increase in irradiation level, the cell temperature rises by approximately 5.4 °C for PV modules with the pancake-shaped collector

[1]Corresponding author.

Contributed by the Solar Energy Division of ASME for publication in the Journal of Solar Energy Engineering: Including Wind Energy and Building Energy Conservation. Manuscript received December 20, 2018; final manuscript received August 6, 2019; published online September 3, 2019. Assoc. Editor: Gerardo Diaz.

and 9.2 °C for PV modules without the pancake-shaped collector. Some reviews of PV/T technologies and their thermal effects can be found in existing publications [10,12,13,18].

Natural and forced convection in vertical and tilted photovoltaic (PV) double-skin systems (open-ended channels) was investigated with reference to BIPVs [19,20]. One numerical study shows that overheating of PV modules occurs and that the cell temperature can reach more than 80 °C near the top of the module when the ambient air is at 20 °C [21]. Various cooling methods have been reviewed for PV modules placed on building rooftops [22]. Flow visualization using hot-wire anemometry measurement was carried out on a model of a double-skin PV façade [23]. A two-inlet BIPV/T system (i.e., an additional air inlet at the middle of the facades, in addition to the top and bottom openings) can increase thermal efficiency by 5% compared with the single inlet at the bottom [20]. Moreover, a metal sheet dividing two compartments of the air cavity behind the BIPV was suggested for improvement of the forced and natural ventilation [24,25]. Han et al. [26,27] carried out a numerical investigation of the double-pane window integrated with see-through a-Si PV cells with low-emittance (low-e) coatings. It was noted that a large quantity of heat transfer indoors caused by radiation can be reduced [27]. In addition to power generation, the air-conditioning cooling load can be reduced [26]. The existing studies are largely based on PV modules with open ends at the top and bottom. To the best knowledge of the authors, the effects of the size of the openings and the air cavity at the back of PV modules have not been fully addressed so far.

Theoretical models were developed for the prediction of electrical and thermal performance of BIPVs [28]. A typical single-pass PV/T was investigated using a numerical model [29]. There is a limited number of studies concerning the cooling effect of the back air cavity or gap on the BIPVs surface temperature. Brandl et al. [30] used the experimental method and CFD simulation to evaluate the thermal behavior and buoyancy-induced airflow characteristics of PV façade elements with fixed side openings. The results showed high PV surface temperature. The induced air flow velocity was less than 0.4 m/s. Gan [21] carried out another numerical study regarding the buoyancy-induced airflow cooling effects of the gap distance between mounted PV panels and the roof and concluded that the temperature of BIPVs decreased with the increase of the gap distance. The critical gap distance stands at about 0.125 m with solar irradiation of 1 kW/m^2 at the ambient temperature of 20 °C. At this critical gap distance, the PV panel's average temperature drops significantly. Further analysis of simulation results by Gan [31] indicated that when the air gap was larger than 0.08 m, the average PV temperature decreased by increasing panel length under buoyancy-induced airflow cooling. Both studies were based on 2D simulations. In his opinion, the BIPV width is much larger than the air gap so the buoyancy-induced flow essentially happens along the length. However, most existing studies ignore external disturbances and wind.

The present study aims to comprehensively investigate the effects of BIPV configurations including the size of the openings and the air cavity behind the BIPV, as well as environmental factors (including wind speed, wind direction, ambient temperature, solar irradiance, etc.) on cell temperature. A numerical analysis is performed using computational fluid dynamics (CFD), and passive cooling methods are studied and evaluated. For the sake of simplicity, the present study isolated a BIPV unit with an air cavity at the back. Cooling effects of various BIPV configurations are discussed, including the size of the openings and cavity depth with natural ventilation at different solar irradiation levels.

2 Methodologies and Simulation Setup

2.1 Computational Fluid Dynamics Simulation Methodology. The present study performs CFD simulations using commercial software with ANSYS FLUENT (version 18.1). Three-dimensional modeling is implemented to investigate the effects of wind speed (u), wind attack angle (θ), solar irradiation (G), and ambient temperature (T_{amb}) on the cell temperature of a PV module. Heat transfer and flow distribution are discussed involving configuration variations, including the size of the openings (at the top and the bottom) and the air cavity depth between the PV module and the wall behind. The modeling involves conduction and convection heat transfers. Nižetić et al. [32] implemented a three-dimensional CFD model to investigate the thermal performance of standalone PV panels involving limited scenarios regarding wind speed, wind attack angle, and solar irradiation conditions on the rooftop. A PV panel was supported with a metal frame and an equivalent thermal energy absorption induced by solar irradiation was applied to PV cells. Several thermal sensors were attached to PV cells and glass surfaces. Cell and surface temperatures of the numerical model were validated experimentally. The said model is extended to the model, proposed in this study, with an air cavity at the back in order to investigate the ventilation of BIPV.

Figure 1 presents the conventional BIPV façade of a building with PV panels installed on the building façade. There is a considerable variation of BIPV designs with or without openings for ventilation. In the present study, the openings between the rows of the PV panels are used for ventilation. While the side edges may be sealed and thus the pressure difference between the two sides of the PV panel may be small or negligible, the thermal effect of the top and bottom openings as well as the air cavity depth between the panels and the back wall are investigated in this study. For the sake of simplicity, a unit model is developed consisting of a PV panel attached to an enclosure with the top and bottom openings as illustrated in Fig. 2.

2.2 Simulation Model Setup. The panel dimensions are based on a typical PV module which is 1600×1000 mm ($L_p \times W_p$) [33] in the unit model. The openings at the top and bottom are of height a and b, respectively, as illustrated in Fig. 2. The air cavity behind the PV panel with the depth d from the wall is also crucial for ventilation. The unit model is placed inside of a fluid domain (i.e., a numerical wind tunnel presented in Fig. 3) for the purposes of fluid dynamics simulation, the dimensions of which are in respect to the length of the panel. The distances of the fluid domain from the inlet and outlet surfaces to the panel are $L = 3L_p$ and $L = 6L_p$, respectively. The domain height and width are $W = H = 7L_p$.

PV panel is made up of several layers of different materials [34] as illustrated in Fig. 2. The front layer is a glass panel whose thickness is 3 mm. The middle layer combines crystalline PV cells and ethylene vinyl acetate (EVA) at a thickness of 0.5 mm, whereas the back layer is 0.5 mm Tedlar. Physical properties of materials for heat transfer in the solid domain including density ρ, thermal

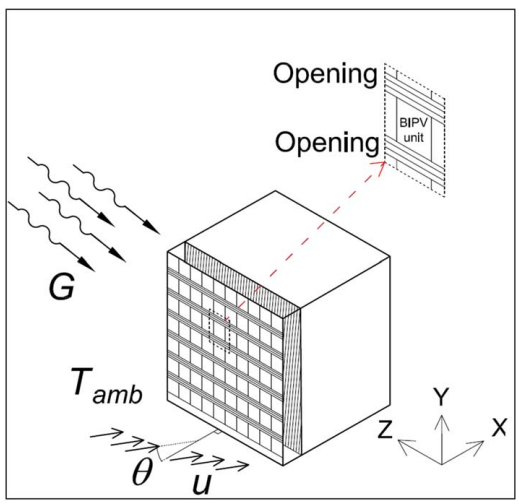

Fig. 1 BIPV façade configuration in the present study

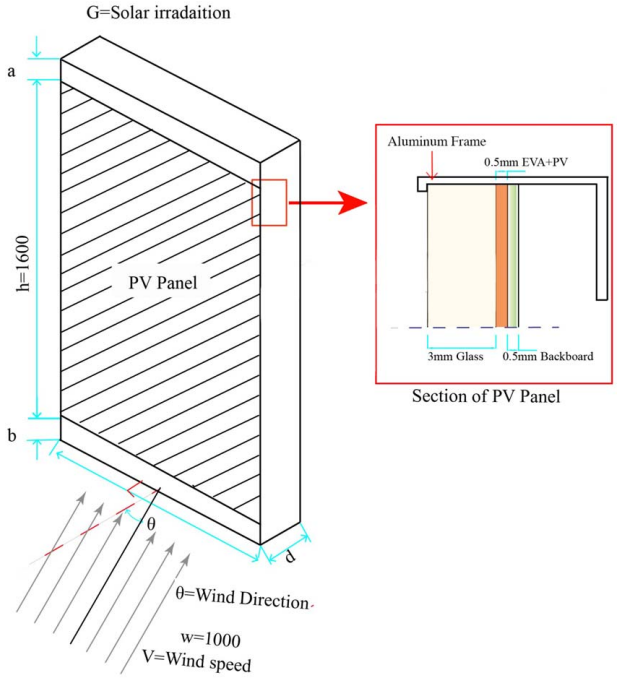

Fig. 2 Typical PV configuration (a unit model)

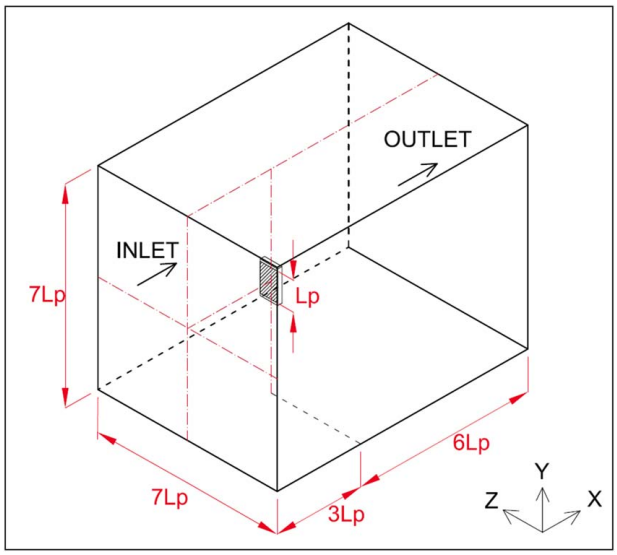

Fig. 3 Numerical wind tunnel in a fluid domain with BIPV unit model

conductivity λ, and specific heat capacity C_p are presented in Table 1. The media of the fluid domain is air at the ambient temperature of 27 °C except in some scenarios that are specified in this study. The specific heat and thermal conductivity of air are 1006.43 J/kg K and 0.0242 W/m K, respectively. Maximum air velocity in the simulation is 4 m/s. Since the Mach number is lower than 0.1 and pressure gradient is low, the flow regime is subsonic and the flow compressibility can be neglected [35,36]. However, the simulation considers the buoyancy effect in relation to the incompressible ideal gas for the air (i.e., the media of fluid domain).

2.3 Meshing. As mentioned above, the thickness of the PV cell is 0.5 mm. To capture heat transfer details of this component, the meshing element height should be less than the thickness of the cell; therefore, the model requires a fine mesh. Comparatively

Table 1 Physical properties of the material

Material	Thermal conductivity λ (W/m K)	Density ρ (kg/m^3)	Specific heat capacity C_p (J/kg K)
Glass	1.04	2500	835
PV	148	2330	705
Tedlar	0.14	1475	1130
Aluminum	225	2700	1028

coarse meshes are set in the air domain in order to reduce computation time and power. The mesh is generated by the ANSYS workbench mesh module. The proximity size function is used with the medium relevance center. The proximity size function sources refer to the faces and edges, whereas the proximity minimum size is 5×10^{-3} m. Maximum face size is 0.535 m and growth rate stands at 1.188. The boundary layer consists of several sublayers in the fluid domain close to solid surfaces. The viscous sublayer, crucial to flow simulation and heat transfer, is immediately adjacent to the wall and the log-layer [37]. Fine mesh is also required on the boundary layer of the fluid domain near to the solid surface where high gradients of temperature and velocity are induced due to the convective heat transfer and buoyancy effect. In order to determine the meshing size of the boundary layer, the present study sets a non-dimensional wall distance $y^+ = 1$ for the wall-bounded flow [38]. Ten inflation layers are used with the growth rate of 1.2 as illustrated in Fig. 4. Based on the 2 m/s wind speed, the height of first inflation layer is set at 0.15 mm. Fine prismatic cells are meshed in the boundary layer and the PV cell. The remaining parts including fluid domain, glass, aluminum frame, and back sheet are meshed with tetrahedral cells of a relatively large size. After meshing, the number of elements reaches 17 million.

Grid independency tests are conducted with for different degrees of freedom (DoF) consisting of approximately 11, 14, 17, and 25 million elements. Figure 5 depicts velocity profiles of four scenarios with different DoF. The profiles are similar. Flow disturbance is generated at the bottom of the air cavity inside the unit where its velocity profile is varied as the number of elements increases. A comparison of the similarity of velocity profiles with 17 and 25 million elements demonstrates that the results tend to be converged when 17 and 25 million elements are involved. Among all four scenarios, the average temperatures of the PV cell surface change within 1 °C and the external velocity profiles are converged (not

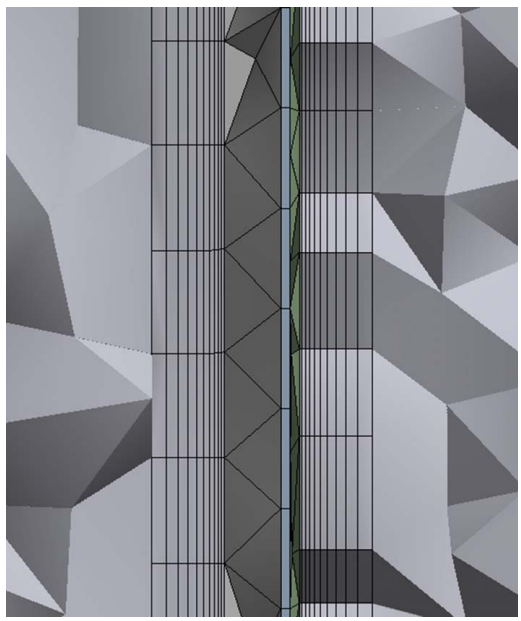

Fig. 4 Mesh of the inflation layers on the solid surface

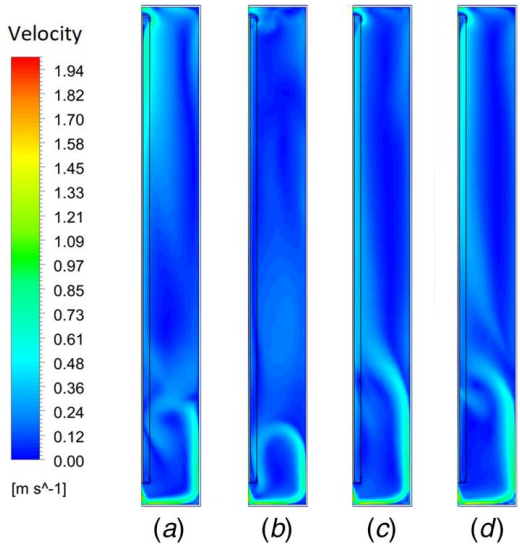

Fig. 5 Section view of air velocity profiles at the central line of the BIPV unit with different number of meshing elements: (*a*) 11 million elements, (*b*) 14 million elements, (c) 17 million elements, and (*d*) 25 million elements

presented herein). Although a more substantial number of elements (or DoF) can achieve higher accuracy, it also increases computational time and power. Since there are limited variations of temperature and velocity profiles between scenarios with 17 and 25 million elements, the former one is selected in this study. The iteration number has also been tested. The buoyancy-induced flow reaches a steady state when the iteration number is around 300 (not presented herein). Therefore, the iteration number was set to 300 in the simulations.

2.4 CFD Algorithms. Shear stress transport (SST) κ-omega turbulent model [39] is used in numerical studies to ensure the accuracy of the convection and possible flow separations. The model is commonly used and it has been experimentally proved that it offers accurate and robust results for a wide range of boundary layer flows with pressure gradient [40]. The SST model is a hybrid turbulence model which combines the advantages of both κ-epsilon and κ-omega models. The κ-omega model is expected to obtain more accurate results for boundary layer flows than κ-epsilon models, while the κ-epsilon model provides an accurate prediction of the flow behavior in the freestream. This numerical model has been proved experimentally with effective prediction of the heat transfers and temperatures of the PV panels under various configurations and environmental conditions [32,41,42], which make the SST κ-omega turbulent model sufficiently realistic for the present study of the PV panel being exposed to open wind conditions. The SST κ-omega model solves the two equations in the model. The κ-omega model was used in the near-wall region extending from the wall to the viscous sublayer, while it switches to κ-epsilon model in the freestream. The SST κ-omega model is based on the Reynolds-averaged Navier–Stokes (RANS) and energy equations [43]. The RANS models can be solved with two transport equations for the turbulent kinetic energy κ and the specific dissipation rate of the turbulent kinetic energy ω [44]. The incompressible flow equations can be given as

$$\text{Continuity equation: } \frac{\partial \langle u_i \rangle}{\partial x_i} = 0, \quad \text{and} \tag{1}$$

$$\text{Momentum equation: } \frac{D\langle u_i \rangle}{Dt} = -\frac{1}{\rho} \cdot \frac{\partial \langle p \rangle}{\partial x_i} + \frac{\partial}{\partial x_j}\left(\nu \frac{\partial \langle u_i \rangle}{\partial x_j} \langle u'_i u'_j \rangle\right) \tag{2}$$

where x_i $(i = x,y,z)$ are the coordinates, u_i and t are the velocity vectors and time, respectively, ν is the dynamic viscosity, and p is the pressure. Equations (1) and (2) are similar to the Navier–Stokes equations, except the time-averaged variables in Eqs. (1) and (2). The Reynolds stresses $-u'_i u'_j$ also must be estimated by turbulence models [45]. The numerical model of PV panel without the back cavity was previously validated by the experiments [32].

The energy equation is given in the following form:

$$\frac{\partial}{\partial t}(\rho E) + \nabla \cdot (u'(\rho E + p)) = \nabla \cdot (k_{eff} \nabla T) \tag{3}$$

where E and ρ are total energy and density, respectively, T is the temperature, and k_{eff} is the effective conductivity. The term on the right-hand side of Eq. (3) represents the energy transfer due to conduction. Detailed expressions of the theories can be found in the theory guide of the ANSYS FLUENT [46].

2.5 Boundary Conditions. The present study considers a BIPV façade under typical tropical outdoor conditions. Wind speed, wind attack angle, ambient temperature, and solar irradiation are investigated. In the model, the freestream wind speed and temperature can be set at the boundary of the inlet. Seven different wind speeds (0 m/s, 0.1 m/s, 0.2 m/s, 0.4 m/s, 1 m/s, 2 m/s, and 4 m/s) are studied based on the weather conditions in Singapore with the annual average wind speed of 2 m/s [47]. In order to apply solar irradiance on the PV module, a simple method is used whereby an equivalent thermal energy absorption is applied on PV cells [32]. The heat flux is equal to the equivalent thermal energy absorption by the PV panel. The BIPV façade equivalent thermal energy absorption from the solar irradiation can be calculated according to Eq. (3)

$$\text{Thermal energy} = 0.74 \times F \times G \tag{4}$$

where F is the sky view factor which represents the ratio between the radiation received by a planar surface and the diffuse irradiance from the sky. Rehman and Siddiqui [48] determined that for a plane with 90 deg tilt angle, F stands at 0.5. Nižetić et al. [32] used the equivalent thermal energy absorption coefficient of 0.74, as can be seen in Eq. (4), which provided highly accurate realistic simulation results compared with experimental results. Peak solar irradiance in Singapore is approximately 1350 W/m^2 [49]. Using Eq. (4), the equivalent BIPV thermal energy absorption under the sun peak hour is 500 W/m^2. In order to study the impact of the solar irradiation variation on BIPV cell temperature, six equivalent thermal energy absorption values of 200, 300, 400, 500, 600, and 700 W/m^2 are investigated. While the wind speed at inlet is set, the outlet boundary condition is set at the outlet in Fig. 3. All other walls in the models are set to be non-slip condition.

3 Results and Discussion

The CFD simulation provides visualization of the temperature and flow distributions under various conditions. The present study discusses the dimensions of ventilation openings, air cavity depth, wind velocity and attack angle, solar irradiation, and ambient temperature. The discussion is separated into two parts. The geometrical configurations of BIPV unit are the first to be investigated. Based on the results of the optimized settings, BIPV performance is evaluated under various environmental conditions.

3.1 Thermal Effect of Even Top and Bottom Opening Dimensions. Initially, the top and bottom openings have the same size (i.e., $a = b$ in Fig. 2) ranging from 30 to 60 mm with a 10 mm interval. Air cavity depth d and wind velocity u are 200 mm and 2 m/s, respectively. In this subsection, the wind attack is considered at normal incidence to PV panels. Figure 6 illustrates PV cell temperature distribution. High temperature occurs at the center top of the panel due to the buoyancy effect.

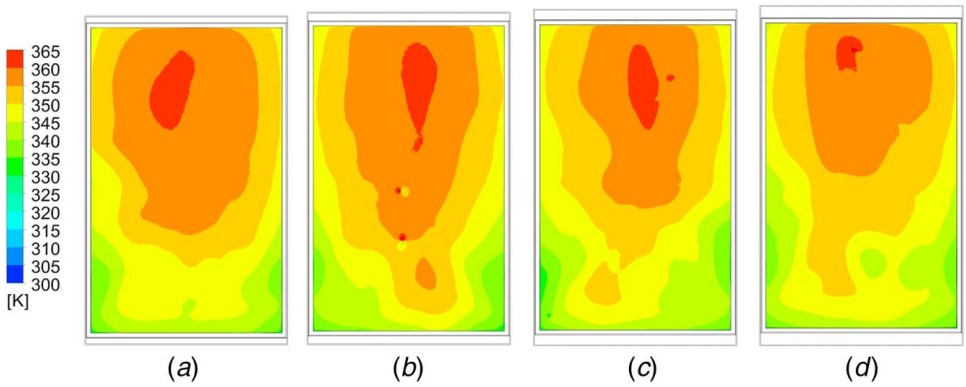

Fig. 6 Front view of the PV cell temperature profile: (*a*) $a = b = 30$ mm, (*b*) $a = b = 40$ mm, (*c*) $a = b = 50$ mm, and (*d*) $a = b = 60$ mm

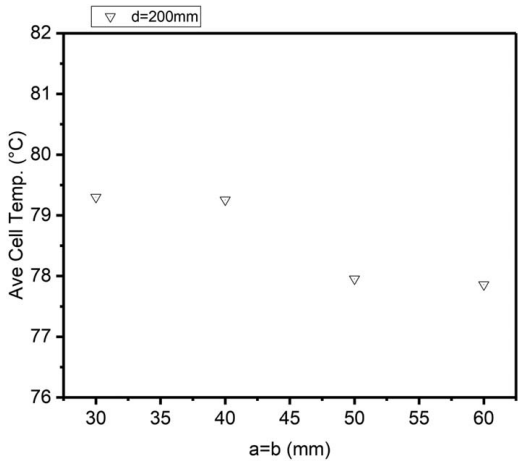

Fig. 7 Average PV cell temperature at 2 m/s wind speed, $d = 200$ mm

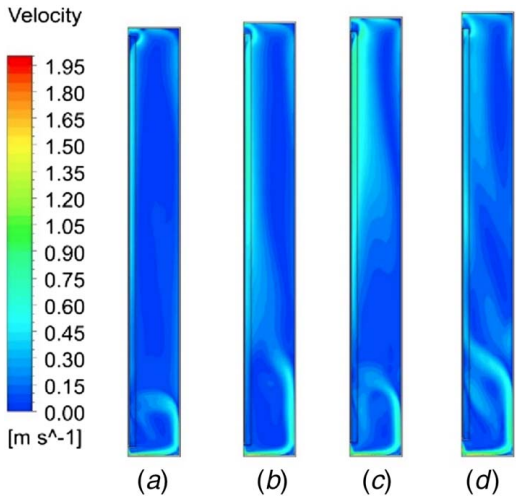

Fig. 8 Section view of air velocity profile at central line of the BIPV unit ($d = 200$ mm) with the equal opening size: (*a*) $a = b = 30$ mm, (*b*) $a = b = 40$ mm, (c) $a = b = 50$ mm, and (*d*) $a = b = 60$ mm

Although the temperature profiles of the four scenarios are different, the average cell temperatures vary within 2 °C range. As presented in Fig. 7, the average temperature is maintained at approximately 79.35 °C for the opening sizes between 30 mm and 40 mm. As a and b increase to 50 mm and 60 mm, the temperature decreases by 1.5 °C. It is noted that there is a power generation drop of approximately 0.45%/K [6,7]. Figure 8 presents sections of the velocity profiles at the vertical centerline of the panel. Velocity profiles are similar at the front of the panel when the openings are of various sizes (not presented herein). Flow disturbance is observed at the bottom of internal air cavity. The maximum flow speed in the air cavity is approximately 0.6 m/s when $a = b = 60$ mm. Limited improvement of cell temperature is observed with the increase of opening sizes when $a = b$ ranges from 30 mm to 60 mm.

3.2 Thermal Effect of Uneven Top and Bottom Openings. Uneven sizes of top and bottom openings may enhance the wind-driven ventilation due to pressure difference at the back of the PV panel inside the air cavity. In order to evaluate the effects of the top and bottom openings sizing ratio on PV cell temperature, six b/a ratios from 1 to 5 have been investigated at a constant wind velocity of 2 m/s and attack angle $\theta = 0$ deg under the equivalent thermal energy absorption of $q = 500$ W/m^2. Preferably, enlarged bottom opening with enhancing the flow in the same direction of buoyancy effect. It is found that there is an insignificant improvement of the PV cell temperature when $b < a$ and thus the results are not discussed here. In this subsection, a and d are kept at the minimum of 30 mm and 200 mm, respectively, while b varies from 30 mm to 150 mm. Figure 9 illustrates the plot of PV cell temperatures with various b/a ratios. Cell temperature slightly decreases as the b/a ratio increases. The temperature drops 2.5 °C when the bottom opening increases from 30 mm to 60 mm (i.e., $b/a = 1$–2). There is a leveling off between 60 mm and 90 mm (i.e., $b/a = 2$–3), while the temperature further drops 1.5 °C when the bottom opening is increased to 150 mm (i.e., $b/a = 5$). Figure 10 presents the velocity profile of six configurations with various b/a ratios. As the b/a ratio increases, flow disturbance gradually forms at the bottom of the air cavity behind the PV panel. This disturbance disrupts the bottom-to-top airflow for heat rejection. It also reduces the convective heat transfer between the back surface of the panel and the air. As the b/a ratio increases, the cooling efficiency becomes higher. The reduction of temperature slows down with a further increase of b.

3.3 Thermal Effect With Various Air Cavity Depths. In the previous subsection, flow disturbance was observed at the bottom of the air cavity. In this subsection, the air cavity depth d is investigated in order to alleviate the adverse effect of the said flow disturbance. Wind velocity, attack angle, and equivalent thermal energy absorption are the same as Sec. 3.2. The selected instance for the various depths study was the one with $a = 30$ mm and $b = 75$ mm (i.e., $b/a = 2.5$). Different cavity depths d are studied ranging from 40 mm to 150 mm. The results are compared with a baseline model of $d = 200$ mm. Figure 11 illustrates how the cavity depth has a significant effect on the airflow inside the cavity. As d

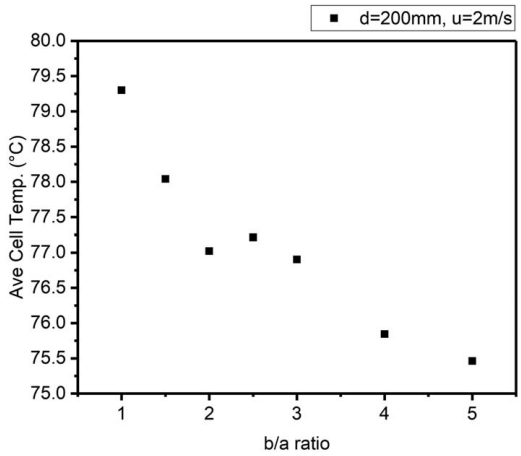

Fig. 9 Plot of the average cell temperature versus *b/a* ratios (*a* = 30 mm, *d* = 200 mm)

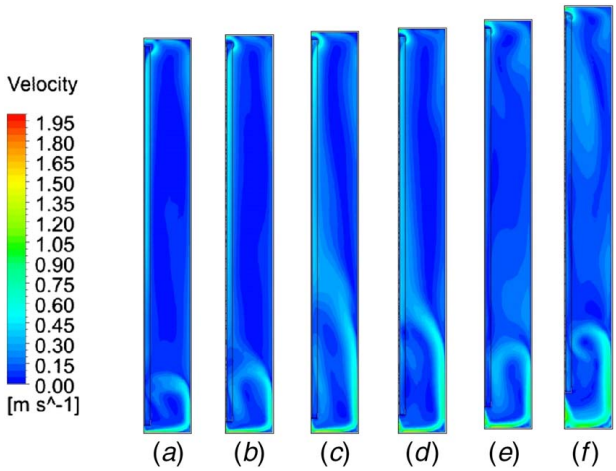

Fig. 10 Air velocity profile around the BIPV unit at various *b/a* ratios (*a* = 30 mm, *d* = 200 mm): (*a*) *b/a* = 1, (*b*) *b/a* = 1.5, (*c*) *b/a* = 2, (*d*) *b/a* = 3, (*e*) *b/a* = 4, and (*f*) *b/a* = 5

decreases from 200 mm to 75 mm, the size of the flow disturbance (at the bottom) and vortex (at the top) is also reduced. When *d* is less than 75 mm, the flow disturbance vanishes. Figure 12(*a*) demonstrates the relationship between PV cell temperature and the cavity depth. High average cell temperature can be observed when *d* is small (for instance, 40 mm). As *d* increases, the temperature drops dipping at around *d* = 100 mm and 125 mm. With further increases of *d,* the temperature also rises and reaches a plateau. Two mechanisms may be governing cell temperature changes at various *d* values. First, the flow resistance between the bottom and top openings of the air cavity increases at small *d* and thus reduces heat transfer efficiency, which this mechanism is dominated for *d* < 100 mm. Second, at large *d* (>100 mm–125 mm), the flow disturbance and vortex induced at the bottom and top of the air cavity, respectively, have adverse effects on the airflow and heat transfer (as presented in Figs. 11(*d*)–11(*f*)). Crossflow ventilation between the two openings is reduced. The second mechanism becomes more significant when *d* > 125 mm. Average cell temperatures are reduced regardless of the size of openings as illustrated in Fig. 12(*b*). It was determined that the average cell temperatures at *d* = 100 mm are lower than those at *d* = 200 mm if other configuration elements are the same.

3.4 Thermal Effect of the Wind Speed. Wind speed is an independent, critical factor in the convective heat transfer. Although the wind speed cannot be controlled in outdoor conditions, its

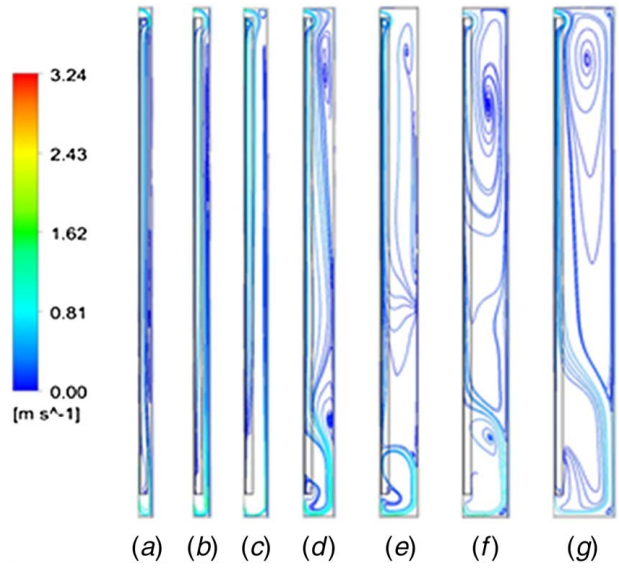

Fig. 11 Internal air streamlines of BIPV units (*a* = 30 mm, *b* = 75 mm) with various cavity depths: (*a*) *d* = 40 mm, (*b*) *d* = 50 mm, (*c*) *d* = 75 mm, (*d*) *d* = 100 mm, (e) *d* = 125 mm, and (*f*) *d* = 200 mm

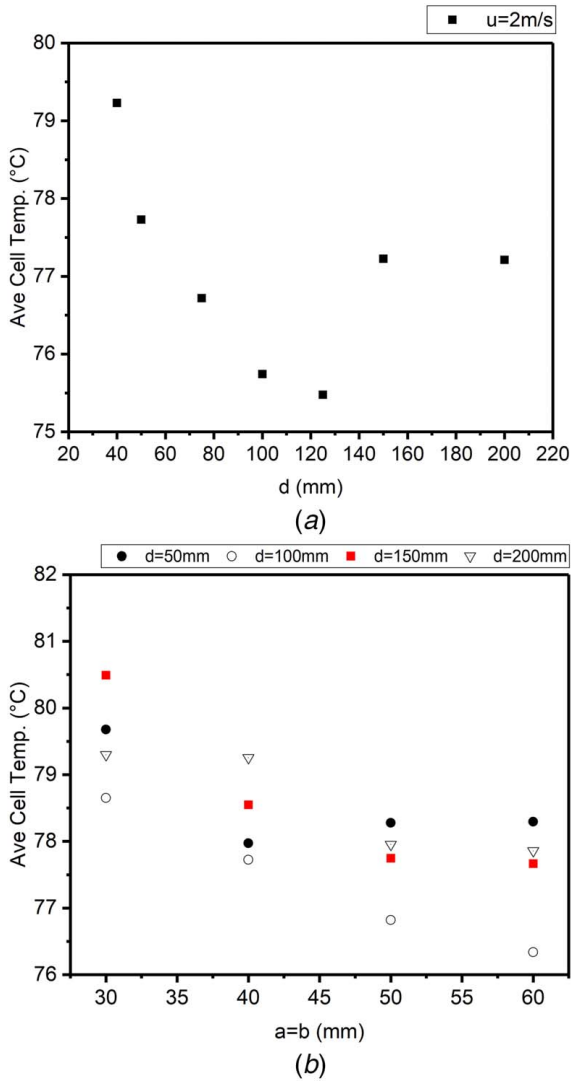

Fig. 12 Average PV cell temperature with various cavity depths with *a* = 30 mm when (*a*) *b/a* = 2.5 and (*b*) *a* = *b*

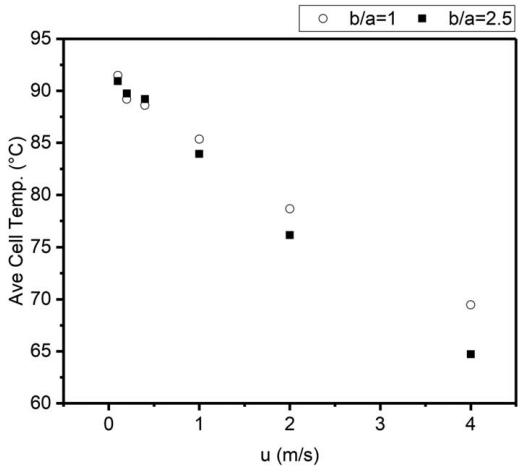

Fig. 13 Average PV panel cell temperature under various wind speeds normal to the PV panel

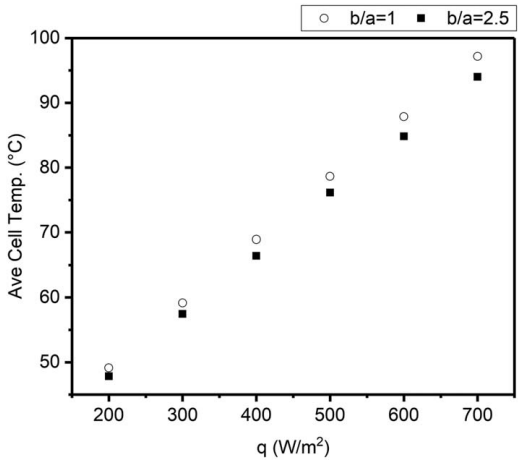

Fig. 14 PV cell temperature versus solar irradiance at a wind speed of $u = 2$ m/s normal to the PV panel

influence is worth investigating in order to estimate BIPV performance. In order to evaluate BIPV performance at different wind speeds, six scenarios with wind velocity ranging from 0.1 to 4 m/s normal to the PV panel were investigated at constant solar irradiance with an equivalent thermal energy absorption of 500 W/m^2. The performance of two BIPV configurations was evaluated and compared. One configuration involves same-sized top and bottom openings (i.e., $a = b = 30$ mm). The other configuration envisages the openings ratio of $b/a = 2.5$ with $a = 30$ mm. In both cases, cavity depth stands at 100 mm.

Figure 13 presents average cell temperatures of configurations with $b/a = 1$ and 2.5 at various wind velocities. At $u = 0.1$ m/s, the temperature in both PV cells is 94 °C. As wind speed increases, the average cell temperature steadily declines. Comparison of the two configurations' geometry reveals that at low wind velocity $u < 1$ m/s, the difference in average cell temperatures is negligible. However, as the wind velocity gradually increases so does the temperature difference. At $u = 4$ m/s, the average cell temperature with $b/a = 2.5$ is 5 °C lower than with $b/a = 1$. It should be noted that the cell temperature on-site should be lower than the results presented since the peak solar irradiance was steadily applied in this numerical experiment. In general, as the wind velocity increases, the average cell temperature decreases almost linearly. However, different BIPV model geometrical configurations will affect the rate of the temperature decrease.

3.5 Effect of the Solar Irradiance. In order to evaluate BIPV cell temperature at various solar irradiance conditions, simulations are carried out with two model configurations ($b/a = 1$ and 2.5, with both $d = 100$ mm) at constant wind speed $u = 2$ m/s normal to the PV panel. Two BIPV unit models are examined when different solar irradiance is applied. The equivalent thermal energy absorption q ranges from 200 to 700 W/m^2. Figure 14 presents the PV cell temperature. As q goes up, an increase in the average cell temperature can be observed. It can also be observed that the average cell temperature has a linear relationship with equivalent thermal energy absorption. A comparison of two sets of results obtained for the plots of $b/a = 1$ and 2.5 revealed a small difference in the average cell temperatures—less than 3 °C. During the peak hour for sun in Singapore when $q = 500$ W/m^2, the average cell temperature is approximately 79 °C. Based on the above observations, it can be concluded that the size of the openings has a limited influence on BIPV performance when solar irradiation is varied.

3.6 Effect of the Wind Attack Angles. Previously mentioned two BIPV model configurations are used in the simulation to investigate BIPV performance with reference to different wind attack

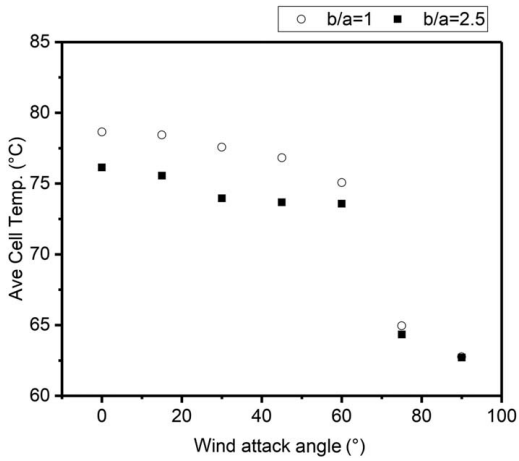

Fig. 15 PV panel cell temperature versus the wind attack angle at $u = 2$ m/s, $a = 30$ mm

angles ranging from $\theta = 0$ deg to 90 deg. Wind velocity and attack angle are 2 m/s and $\theta = 0$ deg, respectively, under the equivalent thermal energy absorption of $q = 500$ W/m^2. Figure 15 presents the average cell temperature at different wind attack angles. For both configurations, when $u = 2$ m/s and $\theta < 60$ deg, the change in temperature is within 3 °C. The panel cell temperature maintains between 74 °C and 79 °C. When 60 deg $< \theta <$ 90 deg, cell temperature drops drastically from 75 °C to 63 °C. It is projected ~5.4% improvement of power generation based on 0.48%/K [6,7]. A comparison of the plots in both instances, with $b/a = 1$ and 2.5, reveals a similar trend. If $\theta < 60$ deg, the general performance of the configuration with $b/a = 2.5$ is better than the one with $b/a = 1$. If $\theta > 60$ deg, then the values of average cell temperatures in both instances are the same. It indicates that the size of the openings has a limited effect on the BIPV performance when $\theta >$ 60 deg. This may be due to the fact that heat rejection is dominated by heat exchange on the front surface of the panel. Figure 16 illustrates a stagnant zone or low velocity in front of the PV panel at $\theta = 0$ deg. Such regions with low wind speed will cause less convection heat transfer and consequently high temperature of PV cell. For $\theta > 60$ deg, increases of the wind speeds are observed on the front surface of the panel. In addition, convection heat transfer should be more effective.

3.7 Effect of the Ambient Temperature. In the actual outdoor conditions, the ambient temperature fluctuates. This may also affect

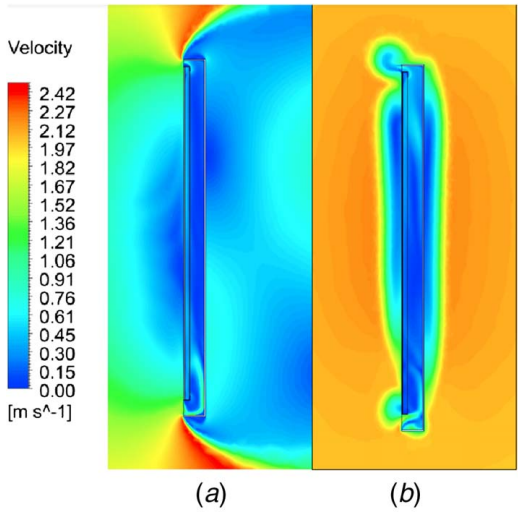

Fig. 16 Comparison of velocity profiles at the panel central section: (*a*) $\theta = 0$ deg and (*b*) $\theta = 90$ deg ($a = b = 30$ mm, $d = 200$ mm, $u = 2$ m/s)

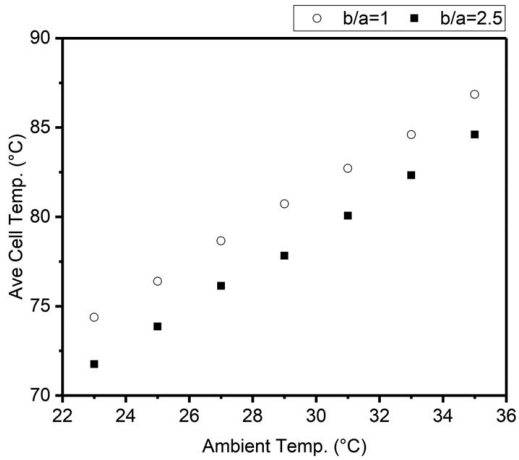

Fig. 17 PV panel cell temperature versus the ambient temperature

BIPV cell temperature. Therefore, seven cases of ambient temperatures are studied when $q = 500$ W/m^2 and $u = 2$ m/s normal to the PV panel. Figure 17 indicates a gradual increase in PV cell temperature as the ambient temperature increases. It has been determined that the average cell temperature stands at $T_{pv} = T_{ambient} + 47.3$ °C (for $b/a = 2.5$ with $a = 30$ mm), and $T_{pv} = T_{ambient} + 50.6$ °C (for $b/a = 1$ with $a = 30$ mm). The ambient temperature change will be the same or similar to the change in average cell temperature. Hence, regardless the opening size, the average cell temperature has a linear relationship with the ambient temperature. However, the size of the openings can affect the average cell temperature. The instance with $b/a = 2.5$ demonstrates lower temperature than the one with $b/a = 1$.

4 Conclusions

CFD simulation is used for the evaluation of the BIPV cooling performance with various geometrical configurations under different environmental conditions. A simplified 3D model of the conventional BIPV is developed. The influence of geometric parameters of the BIPV design on the PV cell temperature is investigated. Geometric parameters include the size of the top and bottom openings and the air cavity depth between the PV back surface and the building wall. The effects of different environmental conditions including wind speed, solar irradiance, wind attack angle, and ambient temperature on the PV cell temperature are investigated.

Increasing the size of both top and bottom openings from 30 mm to 60 mm results in the average temperature decreases by 1.5 °C, which is considered to be less significant. On the other hand, it is determined that the temperature will decrease by increasing the ratio of the bottom-to-top opening sizes, *b/a*. When the *b/a* ratio reaches 5, the temperature drops by 4 °C compared with $b/a = 1$ with $a = 30$ mm. It is projected ~1.92% improvement of power generation based on 0.48%/K from the existing study. Nevertheless, if the air cavity depth is small, the temperature remains high due to flow resistance inside the air cavity. As the air cavity depth increases, the temperature drops, dipping when the air cavity depth is approximately 100 mm–125 mm. If the air cavity depth is further increased, the cell temperature will slightly increase due to flow disturbance and vortex at the bottom and top of the air cavity. The present study identifies the cavity depth between 100 mm and 125 mm as providing the lowest cell temperature.

Two configurations with $b/a = 1$ and 2.5 with $a = 30$ mm are tested under different environmental conditions. As the wind speed increases, the average cell temperature decreases. The cell temperature drops significantly when the wind speed is higher than 1 m/s. If solar irradiance varies, the average cell temperature will exhibit a linear relationship with the solar irradiance regardless of the configuration. If $\theta < 60$ deg, the average cell temperature changes slightly; however, if $\theta > 60$ deg, the temperature drastically drops. The ambient temperature should also be considered. When testing the two BIPV models at different ambient temperatures from 23 °C to 35 °C, the results indicate that the average cell temperature also has a linear relationship with the ambient temperature.

To summarize the above briefly, BIPV configurations influence the average cell temperature and a proper BIPV design can achieve lower cell temperature. When designing BIPV façade, orientation should be considered (since it is related to the wind speed and attack angle). Large wind attack angle, optimal cavity depth, and enlargement of lower opening may have advantages on the reduction of the PV cell temperature. BIPV performance can be assessed since their cell temperature is proportional to the solar irradiance and the ambient temperature.

Acknowledgment

The authors wish to acknowledge the funding support by the research project "Evaluation and Development of Energy Efficient PV Systems in Tropical Environment" [WBS: R-294-000-136-720], which is funded by the NUS-CDL Tropical Technology Laboratory (T2 Lab) and City Development Limited. The authors would like to thank the Department of Architecture, School of Design and Environment, National University of Singapore for the support of this project. The comments and helps from Prof. Sandro Nižetić are appreciated. The authors also thank Miss. Zhuoli Wang and Mr. Xiang Zhang for their help with simulations.

References

[1] Razykov, T. M., Ferekides, C. S., Morel, D., Stefanakos, E., Ullal, H. S., and Upadhyaya, H. M., 2011, "Solar Photovoltaic Electricity: Current Status and Future Prospects," Sol. Energy, **85**(8), pp. 1580–1608.
[2] Shanmugavalli, K. R., and Vedamuthu, R., 2015, "Viability of Solar Rooftop Photovoltaic Systems in Grouphousing Schemes," Curr. Sci., **108**(6), pp. 1080–1085.
[3] Singh, R., and Banerjee, R., 2015, "Estimation of Rooftop Solar Photovoltaic Potential of a City," Sol. Energy, **115**, pp. 589–602.
[4] Luther, J., Reindl, T., Wang, D., Aberle, A., Walsh, W., Nobre, A., and Yao, G., 2013, *Solar Photovoltaic (PV) Roadmap for Singapore (A Summary)*, Solar Energy Research Institute of Singapore (SERIS), Singapore. https://www.nccs.gov.sg/docs/default-source/default-document-library/solar-photovoltaic-roadmap-for-singapore-a-summary.pdf
[5] Radziemska, E., 2003, "The Effect of Temperature on the Power Drops in Crystalline Silicon Solar Cells," Renew. Energy, **28**(1), pp. 1–12.
[6] Candanedo, L. M., Athienitis, A., and Park, K.-W., 2011, "Convective Heat Transfer Coefficients in a Building-Integrated Photovoltaic/Thermal System," ASME J. Sol. Energy Eng., **133**(2), p. 021002.

[7] Zondag, H. A., 2008, "Flat-Plate PV-Thermal Collectors and Systems: A Review," Renew. Sustain. Energy Rev., **12**(4), pp. 891–959.
[8] Park, K. E., Kang, G. H., Kim, H. I., Yu, G. J., and Kim, J. T., 2010, "Analysis of Thermal and Electrical Performance of Semi-Transparent Photovoltaic (PV) Module," Energy, **35**(6), pp. 2681–2687.
[9] Agrawal, B., and Tiwari, G. N., 2011, "An Energy and Exergy Analysis of Building Integrated Photovoltaic Thermal Systems," Energy Sources Part A, **33**(7), pp. 649–664.
[10] Abdul Hamid, S., Yusof Othman, M., Sopian, K., and and Zaidi, S. H., 2014, "An Overview of Photovoltaic Thermal Combination (PV/T Combi) Technology," Renew. Sustain. Energy Rev., **38**, pp. 212–222.
[11] Li, W., Paul, M. C., Rolley, M., Sweet, T., Gao, M., Baig, H., Fernandez, E. F., Mallick, T. K., Montecucco, A., Siviter, J., Knox, A. R., Han, G., Gregory, D. H., Azough, F., and Freer, R., 2017, "A Coupled Optical-Thermal-Electrical Model to Predict the Performance of Hybrid PV/T-CCPC Roof-Top Systems," Renew. Energy, **112**, pp. 166–186.
[12] Noro, M., Lazzarin, R., and Bagarella, G., 2016, "Advancements in Hybrid Photovoltaic-Thermal Systems: Performance Evaluations and Applications," Energy Procedia, **101**, pp. 496–503.
[13] Sathe, T. M., and Dhoble, A. S., 2017, "A Review on Recent Advancements in Photovoltaic Thermal Techniques," Renew. Sustain. Energy Rev., **76**, pp. 645–672.
[14] Slimani, M. E. A., Amirat, M., Kurucz, I., Bahria, S., Hamidat, A., and Chaouch, W. B., 2017, "A Detailed Thermal-Electrical Model of Three Photovoltaic/Thermal (PV/T) Hybrid Air Collectors and Photovoltaic (PV) Module: Comparative Study Under Algiers Climatic Conditions," Energy Convers. Manage., **133**, pp. 458–476.
[15] Adeli, M. M., Sobhnamayan, F., Farahat, S., Alavi, M. A., and Sarhaddi, F., 2012, "Experimental Performance Evaluation of a Photovoltaic Thermal (PV/T) Air Collector and Its Optimization," Strojniški vestnik—J. Mech. Eng., **58**(5), pp. 309–318.
[16] Corbin, C. D., and Zhai, Z. J., 2010, "Experimental and Numerical Investigation on Thermal and Electrical Performance of a Building Integrated Photovoltaic–Thermal Collector System," Energy Build., **42**(1), pp. 76–82.
[17] Nahar, A., Hasanuzzaman, M., and Rahim, N. A., 2017, "A Three-Dimensional Comprehensive Numerical Investigation of Different Operating Parameters on the Performance of a Photovoltaic Thermal System With Pancake Collector," ASME J. Sol. Energy Eng., **139**(3), p. 031009.
[18] Bahaidarah, H. M. S., Baloch, A. A. B., and Gandhidasan, P., 2016, "Uniform Cooling of Photovoltaic Panels: A Review," Renew. Sustain. Energy Rev., **57**, pp. 1520–1544.
[19] Lau, G. E., Sanvicente, E., Yeoh, G. H., Timchenko, V., Fossa, M., Ménézo, C., and Giroux-Julien, S., 2012, "Modelling of Natural Convection in Vertical and Tilted Photovoltaic Applications," Energy Build., **55**, pp. 810–822.
[20] Yang, T., and Athienitis, A. K., 2015, "Experimental Investigation of a Two-Inlet Air-Based Building Integrated Photovoltaic/Thermal (BIPV/T) System," Appl. Energy, **159**, pp. 70–79.
[21] Gan, G., 2009, "Numerical Determination of Adequate Air Gaps for Building-Integrated Photovoltaics," Sol. Energy, **83**(8), pp. 1253–1273.
[22] Chandrasekar, M., Rajkumar, S., and Valavan, D., 2015, "A Review on the Thermal Regulation Techniques for Non Integrated Flat PV Modules Mounted on Building top," Energy Build., **86**, pp. 692–697.
[23] Zogou, O., and Stapountzis, H., 2012, "Flow and Heat Transfer Inside a PV/T Collector for Building Application," Appl. Energy, **91**(1), pp. 103–115.
[24] Ameri, M., Mahmoudabadi, M. M., and Shahsavar, A., 2012, "An Experimental Study on a Photovoltaic/Thermal (PV/T) Air Collector With Direct Coupling of Fans and Panels," Energy Sources Part A, **34**(10), pp. 929–947.
[25] Shahsavar, A., Ameri, M., and Gholampour, M., 2012, "Energy and Exergy Analysis of a Photovoltaic-Thermal Collector With Natural Air Flow," ASME J. Sol. Energy Eng., **134**(1), p. 011014.
[26] Han, J., Lu, L., Peng, J., and Yang, H., 2013, "Performance of Ventilated Double-Sided PV Façade Compared With Conventional Clear Glass Façade," Energy Build., **56**, pp. 204–209.
[27] Han, J., Lu, L., and Yang, H., 2010, "Numerical Evaluation of the Mixed Convective Heat Transfer in a Double-Pane Window Integrated With See-Through a-Si PV Cells With Low-e Coatings," Appl. Energy, **87**(11), pp. 3431–3437.
[28] Shan, F., Tang, F., Cao, L., and Fang, G., 2014, "Comparative Simulation Analyses on Dynamic Performances of Photovoltaic–Thermal Solar Collectors With Different Configurations," Energy Convers. Manage., **87**, pp. 778–786.
[29] Amori, K. E., and Taqi Al-Najjar, H. M., 2012, "Analysis of Thermal and Electrical Performance of a Hybrid (PV/T) Air Based Solar Collector for Iraq," Appl. Energy, **98**, pp. 384–395.
[30] Brandl, D., Mach, T., Grobbauer, M., and Hochenauer, C., 2014, "Analysis of Ventilation Effects and the Thermal Behaviour of Multifunctional Façade Elements With 3D CFD Models," Energy Build., **85**, pp. 305–320.
[31] Gan, G., 2009, "Effect of Air Gap on the Performance of Building-Integrated Photovoltaics," Energy, **34**(7), pp. 913–921.
[32] Nižetić, S., Grubišić-Čabo, F., Marinić-Kragić, I., and Papadopoulos, A. M., 2016, "Experimental and Numerical Investigation of a Backside Convective Cooling Mechanism on Photovoltaic Panels," Energy, **111**, pp. 211–225.
[33] SUNMetrix, 2017, "Sunmetrix Solar Panel Size for Residential, Commercial and Portable Applications," http://sunmetrix.com/solar-panel-size-for-residential-commercial-and-portable-applications/, Accessed August 25, 2019.
[34] Wohlgemuth, J. H., 2012, "Standards for PV Modules and Components—Recent Developments and Challenges (No. NREL/CP-5200-56531)," 27th European Photovoltaic Solar Energy Conference and Exhibition, U.S. Department of Commerce National Technical Information Service, National Renewable Energy Lab (NREL), Golden, CO.
[35] Çengel, Y. A., and Cimbala, J. M., 2014, *Fluid Mechanics Fundamentals and Applications*, McGraw-Hill, New York.
[36] Chen, H. C., Patel, V. C., and Ju, S., 1990, "Solutions of Reynolds-Averaged Navier-Stokes Equations for Three-Dimensional Incompressible Flows," J. Comput. Phys., **88**(2), pp. 305–336.
[37] Von Karman, T., 1931, "*Mechanical Similitude and Turbulence*," NACA Technical Memorandum 611. No. NACA-TM-611, National Advisory Committee for Aeronautics, Washington, DC.
[38] ANSYS, 2017, *18.1 ANSYS Fluent Theory Guide*, ANSYS.
[39] Menter, F. R., 1994, "Two-Equation Eddy-Viscosity Turbulence Models for Engineering Applications," AIAA J., **32**(8), pp. 1598–1605.
[40] Menter, F. R., 1993, "Zonal Two Equation Kappa-Omega Turbulence Models for Aerodynamic Flows," 23rd Fluid Dynamics, Plasmadynamics, and Lasers Conference, NASA Ames Research Center, Orlando, FL, p. 2906.
[41] Brinkworth, B. J., Cross, B. M., Marshall, R. H., and Yang, H., 1997, "Thermal Regulation of Photovoltaic Cladding," Sol. Energy, **61**(3), pp. 169–178.
[42] Raval, H. D., Maiti, S., and Mittal, A., 2014, "Computational Fluid Dynamics Analysis and Experimental Validation of Improvement in Overall Energy Efficiency of a Solar Photovoltaic Panel by Thermal Energy Recovery," J. Renew. Sustain. Energy, **6**(3).
[43] Xamán, J., Álvarez, G., Lira, L., and Estrada, C., 2005, "Numerical Study of Heat Transfer by Laminar and Turbulent Natural Convection in Tall Cavities of Façade Elements," Energy Build., **37**(7), pp. 787–794.
[44] Kanargi, O. B., Lee, P. S., and Yap, C., 2017, "A Numerical and Experimental Investigation of Heat Transfer and Fluid Flow Characteristics of a Cross-Connected Alternating Converging–Diverging Channel Heat Sink," Int. J. Heat Mass Transfer, **106**, pp. 449–464.
[45] Yuan, C., and Ng, E., 2012, "Building Porosity for Better Urban Ventilation in High-Density Cities—A Computational Parametric Study," Build. Environ., **50**, pp. 176–189.
[46] ANSYS Fluent, 2017, *Theory Guide*, ANSYS Inc., Canonsburg, PA.
[47] Meteorological Service Singapore, 2010, "Climate of Singapore," http://www.weather.gov.sg/climate-climate-of-singapore/, Accessed August 25, 2019.
[48] Rehman, N. u., and Siddiqui, M. A., 2015, "A Novel Method for Determining Sky View Factor for Isotropic Diffuse Radiations for a Collector in Obstacles-Free or Urban Sites," J. Renew. Sustain. Energy, **7**(3), p. 033110.
[49] NSR, 2018, "National Solar Repository of Singapore (NSR)," http://www.solar-repository.sg/local-weather, Accessed August 25, 2019.